Torsional progressive damage mechanisms in 3-D braided carbon fiber/ epoxy resin composite tubes

Xun, Limeng; Mosleh, Yasmine; Sun, Baozhong; Pascoe, John-Alan; Gu, Bohong

DOI
10.1016/j.compscitech.2024.110615

Publication date
2024

Document Version
Final published version

Published in
Composites Science and Technology

Composites Science and Technology 252 (2024) 110615

Contents lists available at ScienceDirect

Composites Science and Technology

journal homepage: www.elsevier.com/locate/compscitech

Torsional progressive damage mechanisms in 3-D braided carbon fiber/epoxy resin composite tubes

Limeng Xun [a,c], Yasmine Mosleh [b], Baozhong Sun [a], John-Alan Pascoe [c,**], Bohong Gu [a,*]

[a] Shanghai Frontiers Science Center of Advanced Textiles, College of Textiles, Donghua University, Shanghai, 201620, China
[b] Biobased Structures and Materials Group, Department of Engineering Structures, Faculty of Civil Engineering and Geosciences, Delft University of Technology, Delft, Netherlands
[c] Department of Aerospace Structures and Materials, Faculty of Aerospace Engineering, Delft University of Technology, Delft, Netherlands

ARTICLE INFO

Keywords:
Polymer-matrix composites (PMCs)
Fracture
Finite element analysis (FEA)
Braiding

ABSTRACT

3-D braided composites are a promising material for manufacturing tubular structures. However, a thorough understanding of their damage mechanisms under torsion is required to maximize their potential applications. The present work constructed a multiscale equivalent model, integrating mesoscopic and homogeneous structures to reveal torsional behavior of 3-D braided carbon fiber/epoxy resin composite tubes. The cumulative failure process, spatial stress distribution and interface damage were calculated to illustrate stress transfer and damage initiation and propagation. It is found that stress varies on the surface and internally within the representative unit cell (RUC). The yarns experience both axial tension parallel to the direction of torsion and axial compression perpendicular to the direction of torsion. The stress difference between them leads to damage initiation and propagation. Interfacial cracking as main damage mode hinders the stress transfer between resin and fiber bundles. The results show that the braided yarn path, axial stress dispersion in two directions and localization of damage effectively impede the torsional damage propagation.

1. Introduction

3-D braided composites feature fibers interlacing in three dimensions to form continuous structures, granting them superior strength and stiffness as well as greater damage resistance [1–6]. Torsion is an often occurred loading for tube structures such as driven shaft in vehicles and aircrafts [7,8]. The remarkable torsional properties of 3-D braided composite tubes provide durability and lightweight solutions that help improve the performance of the vehicles and aircrafts [9,10].

Examining the progressive damage mechanisms during torsion is vital to take full advantage of the 3-D braided composite tubes [11]. The macroscopic torsional behaviors have been gradually revealed by relying on advanced experimental techniques in existing studies [12]. The development of surface strain and cracks can be monitored using the 3D-digital image correlation (DIC) technique [13,14]. Cumulative damage modes can be recognized by the frequency of acoustic emission (AE) signals [15–17]. Damage morphologies and their statistical quantification following failure can be captured with the assistance of micro-computed tomography (Micro-CT) [13,18]. Temperature changes resulting from failure can be measured with thermography analysis to unveil the damage propagation [19]. While these damage features have been mapped, the complexity of the 3-D braided structure still makes it challenging to understand how the internal microstructure affects the macroscopic performance.

The development of multi-scale finite element analysis (FEA) methods has provided new perspectives for studying the mechanical behaviors [20–25]. The braided composites exhibit a periodic structure, which can be characterized by a Representative Volume Element (RVE). Previously, Zhang et al. [26] have successfully predicted the elastic constants of 3-D tubular braided composites through simulating RVE behaviors. The correlation between braiding parameters and torsional performance also can be investigated by a microscopic unit cell model [27,28]. Gong et al. [29] established an orthogonal anisotropic tubular macro-model to predict the torsional strength and stiffness of a 3-D braided composite drive shaft. Researches indicate that initial damage occurs at the fiber/matrix interface. As applied loading increases, the matrix damage expands and connects between interfaces, eventually resulting in failure. Despite the above-mentioned results, the current

* Corresponding author.
** Corresponding author.
E-mail addresses: j.a.pascoe@tudelft.nl (J.-A. Pascoe), gubh@dhu.edu.cn (B. Gu).

https://doi.org/10.1016/j.compscitech.2024.110615
Received 29 December 2023; Received in revised form 16 March 2024; Accepted 17 April 2024
Available online 18 April 2024

investigations primarily concentrate on the impact of raw materials, loading conditions, and braiding structural parameters, etc., on the macroscopic torsional behaviors [13,30,31]. Investigations into the torsional spatial stress distribution, interfacial, and crack initiations and extensions are limited.

This study is a comprehensive effort to unveil the damage imitations and propagations of the 3-D braided composite tubes. The structure-performance relationship and damage mechanisms were revealed by progressive damage modelling. The evolution of damage, distribution of internal stress and interfacial damage are described by transferring torsional responses from the macro-scale to the meso-scale, considering the multi-scale characteristics inherent in braided structures. Additionally, the 3D-DIC and micro-CT techniques are combined to understand shear strain and damage morphologies, verify the accuracy of FEA. This research focuses on a relatively unexplored aspect, enhancing our understanding of torsional properties and contributing to the optimization of tube behaviors.

2. Multi-scale modelling

2.1. Geometric model

The mesoscale geometric model of 3-D braided carbon fiber/epoxy resin composite tube consists of tubular yarns (impregnated carbon fiber bundles) preform and epoxy resin matrix. The preform was braided through 1 × 1 four-step braiding process. The geometric arrangement of fiber bundles cycling from the inside to the outside in 3D space is determined from the trajectory of yarn carriers, as depicted in Fig. 1(a) (b). The meso-scale model is derived from RUC arrays. The RUC array comprises an inner unit cell and a surface unit cell, with the surface unit cell further divided into an internal surface unit cell and an outside surface unit cell. The RUC height is 6 mm. Fig. 1(c) shows the RUC solid model, drawn with CATIA V5R20 software. The developed multiscale model, which consists of a meso-scale model component around the failure area and homogenized macro-scale model components at both ends, is illustrated in Fig. 1(d). The homogeneous model spans 2 × 35 mm and the mesoscale model measures 50 mm.

2.2. Constitutive models and damage criteria

The epoxy resin and braided yarns are modelled as isotropic and transversely isotropic materials, respectively. The bridging model [32] was used to calculate the stresses of constituents of the 3-D braided composites. In the bridging model, each segment has its own local coordinate system (1-2-3): 1 is the fiber direction and the 2–3 is the cross-section perpendicular to the 1 direction. Table 1 lists the material properties of carbon fiber, epoxy resin and braided yarn. The properties of the carbon fiber, and epoxy resin were provided from the manufacturers. The mechanical properties of the yarns in the local coordinate system then need to be transferred to the global coordinate system, by Eq. (1)

$$\left[\mathrm{S}_y\right]_g = \left[T_{ij}\right]_c \left[\mathrm{S}_y\right]_l \left[T_{ij}\right]_c^T \tag{1}$$

where $[T_{ij}]_c$ is a generalized rotation matrix. $[\mathrm{S}_y]_g$ is the global compliance matrix of the yarn, $[S_y]_l$ is the local compliance matrix of the yarn. Fig. 1(c) shows the conversion relationships between local and global coordinate systems. In the meso-scale model component, the global compliance matrix of individual unit cells in the global coordinate system is obtained using the volume averaging method [26]. The stiffness matrix of yarns $[C_y]_g^{total}$ can be expressed as Eq. (2):

$$\left[C_y\right]_g^{total} = \sum V_y^{ij} \left[C_y\right]_g^{ij} \left[C_y\right]_g = inv\left(\left[S_y\right]_g\right) \tag{2}$$

where V_y is the volume of yarn in an individual unit cell. The compliance matrix of the homogenous component is given by Eq. (3):

$$[S] = inv\left(V_y \left[C_y\right]_g^{total} + \left(1 - V_y\right)[C]^m\right) \tag{3}$$

For damage modelling, the ductile and shear criterion mode [33] is implemented here. This model assumes that damage initiation occurs when the following condition is met:

$$\omega_i = \int \frac{\mathrm{d}\bar{\varepsilon}^{pl}}{\bar{\varepsilon}_{\mathrm{i}}^{pl}\left(\sigma_{\mathrm{i}}, \dot{\bar{\varepsilon}}^{pl}\right)} = 1 i = D, S \tag{4}$$

where ω_{i} is a state variable that increases monotonically with plastic deformation, $\dot{\bar{\varepsilon}}^{pl}$ is equivalent plastic strain rate, D, S refer to ductile and

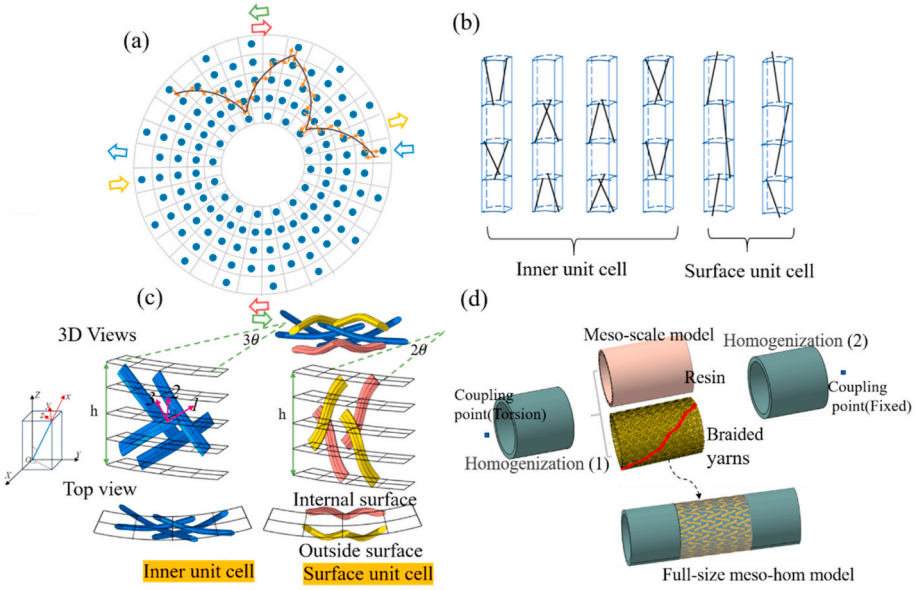

Fig. 1. Multi-scale geometric model of 3-D braided composite tube. (a) Trajectory projection of carbon fiber bundles in 3D four-step braiding process. Columns (n) is 32 and layers (m) is 3. (b) Geometrical relations of braided bundles in 3D space. (c) Solid models of inner unit cell and surface unit cell. (d) Equivalent model integrating homogenizations and meso-scale model.

Table 1
The material properties of carbon fibre, epoxy resin and braided yarns.

	E_{11} (GPa)	$E_{22} = E_{33}$ (GPa)	$G_{12} = G_{13}$ (GPa)	G_{23} (GPa)	$\nu_{12} = \nu_{13}$	ν_{23}	Density (g/cm^3)
Epoxy resin	2.4		0.89		0.35		1.13
Carbon fiber	230	14	9	5	0.25	0.3	1.8
Yarns	169.49	8.13	3.59	2.77	0.25	0.42	1.62

shear, respectively. The equivalent plastic strain $\overline{\varepsilon}_{\mathrm{D}}^{pl}$ is a function of stress triaxiality η and $\overline{\varepsilon}_{\mathrm{S}}^{pl}$ is a function of shear stress ratio θ_s and strain rate:

$$\overline{\varepsilon}_{\mathrm{D}}^{pl}\left(\eta, \dot{\overline{\varepsilon}}^{pl}\right)\ \overline{\varepsilon}_{\mathrm{S}}^{pl}\left(\theta_s, \dot{\overline{\varepsilon}}^{pl}\right) \tag{5}$$

Damage initiation leads to a gradual degradation of material stiffness, following the specified damage evolution. The damage evolution law utilized in ductile and shear failure relies on dissipated energy during the damage process, resulting in mesh element removal upon material failure. At any given time during the analysis, the stress tensor in the material is given by the scalar damage equation:

$$\sigma = (1 - D)\overline{\sigma} \tag{6}$$

where $\overline{\boldsymbol{\sigma}}$ is the undamaged stress tensor computed in the current increment. The overall damage variable, $0 \leq \mathrm{D} \leq 1$, captures the combined effect of all active damage mechanisms leading to material failure.

We adopted a surface-based cohesive zone model (CZM) to model interface damage between yarns and resin matrix. The linear elastic traction-separation model provided with commercial finite element software ABAQUS for interface nodes assumes linear elastic behavior initially, followed by damage initiation and evolution. The elastic behavior can then be written as:

$$\mathrm{T} = \begin{Bmatrix} T_n \\ T_s \\ T_t \end{Bmatrix} = \begin{bmatrix} K_{nn} & K_{ns} & K_{nt} \\ K_{ns} & K_{ss} & K_{st} \\ K_{nt} & K_{st} & K_{tt} \end{bmatrix} \begin{Bmatrix} \delta_n \\ \delta_s \\ \delta_t \end{Bmatrix} = \mathrm{K}\delta \tag{7}$$

where **T** and δ are traction vector and separations respectively. *n, s, t* represents the normal and two shear components. **K** is the initial modulus of the interface. Damage can occur once the damage initiation criterion given by Eq. (8) is met:

$$\max\left\{\frac{\langle t_n \rangle}{t_n^o}, \frac{t_s}{t_s^o}, \frac{t_t}{t_t^o}\right\} = 1 \tag{8}$$

where t_n^o, t_s^o, t_t^o refer to the peak values of the interface contact traction at separation in the normal and two shear directions, respectively. Upon reaching the corresponding initiation criterion, the cohesive stiffness is degraded. The damage evolution under the mixed-mode condition is defined as follows:

$$K = (1 - D)\overline{K} \tag{9}$$

The damage variable D increases from 0 to 1 after damage initiation upon further loading. $\overline{K}$ refers to the initial stiffness matrix. Following damage initiation, the Benzeggagh Kenane (B–K) fracture criterion based on fracture energy, expressed by Eq. (10), is employed to describe the progression of damage.

$$G_n^C + \left(G_s^C - G_n^C\right)\left\{\frac{G_S}{G_T}\right\}^{\eta} = G^C \tag{10}$$

where G_n^C, G_s^C, G_t^C refer to the critical fracture energies required to cause failure in the normal, the first, and the second shear directions, respectively. η is a cohesive property parameter. Table 2 gives the interfacial parameters used in the model.

Table 2
Interfacial parameters of surface-based cohesive behaviours model.

K_n (N/mm3)	$K_s = K_t$ (N/mm3)	t_n^0 (MPa)	$t_s^0 = t_t^0$ (MPa)	G_n^c (N/mm)	$G_s^c = G_t^c$ (N/mm)	β
4×10^6	1×10^6	120	150	0.8	1.2	1.0

2.3. Modelling discretization and interaction

The numerical calculations were performed using ABAQUS version 6.14–4. The yarns were discretized with C3D8R element type (8 node solid brick elements with reduced integration points) with scanning mesh technique. The yarn model mesh size was 0.35 mm. The resin component within the meso-scale model component was discretized into the C3D4 element type (4 node solid brick elements) with free meshing techniques. The resin model mesh size was 0.5 mm. The macro-scale homogeneous model component was discretized using co-node scanning mesh technique applied to the contact surfaces with the mesoscale model. The boundary conditions were depicted in Fig. 1(d).

3. Specimen preparation and tests

3.1. Manufacturing of thin-walled tubes

The 3-D braided composite thin-walled tubes were fabricated using carbon fiber bundles (SYT49S–12K from Zhongfu Shenying Carbon Fiber Co., Ltd, China) and JC-02A/JC-02B epoxy resin (provided by Changshu Jiafa Chemical Inc, China). Fig. 1(a) shows the braiding process. Resin impregnation was accomplished by vacuum-assisted resin transfer molding. Afterward, the composite underwent curing at 90 °C for 2 h, followed by 110 °C for 1 h and 130 °C for 4 h. The specimens were polished and cut to the size of 30.70 mm (inner diameter) × 2.25 mm (wall thickness). The fiber volume fraction is 35.2 ± 2 %. The braiding angle is 45°. Fig. 2 (a) shows an optical micrograph of a tubular specimen.

3.2. Torsional experiments and characterization techniques

Static torsion tests were carried out with MTS System equipment (CTT1503) applying twist at a torsion angle rate of 6°/min. Load was applied until the specimen failed. In total, five specimens were tested. A 3D-DIC system aided in revealing the evolution of shear strain ($\varepsilon_{\mathrm{xy}}$). The speckles were formed by some black paint spots sprayed randomly on a white paint background before testing. Images were captured at a rate of 10 frames/s. An in-depth analysis by micro-CT was employed for failure specimens to obtain spatial damage characteristics. Fig. 2 (b) shows the test set-up.

4. Results and discussions

4.1. Validation of the multiscale model

The torque-torsion angle curves (Fig. 3) exhibited a linear upward trend under torsional loading, indicating that the material undergoes elastic deformation. The critical torque and torsion angle were 587.24 N*m and 8.28°, respectively. After reaching the critical torsion angle, the torque rapidly declined and the tube lost its load-bearing capacity. 3-D stereo images of the failed specimens were obtained by employing micro-CT (Fig. 3(b)). The damage volume was 2.13 %. The damage showed a spiral pattern (regions marked in red) propagating along the pipe wall. As shown in Fig. 3, the results of the FEA matched the

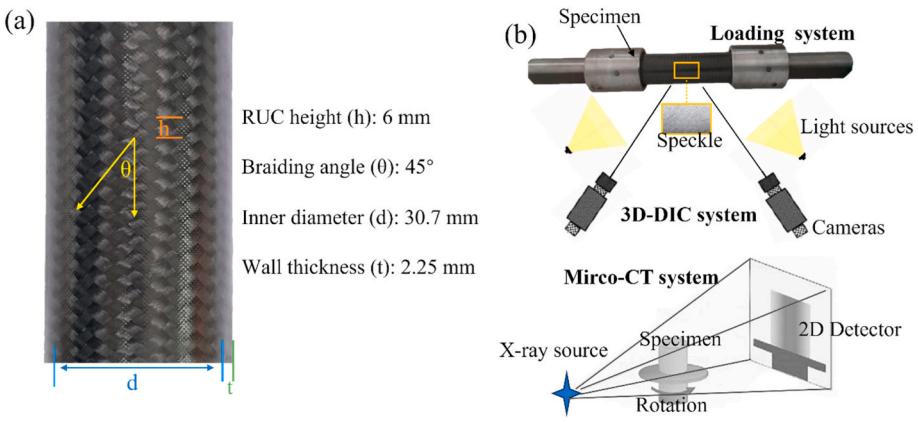

Fig. 2. Specimen and test set-up. (a) Optical micrograph of a tubular specimen. (b) Test systems of loading, 3D-DIC and micro-CT.

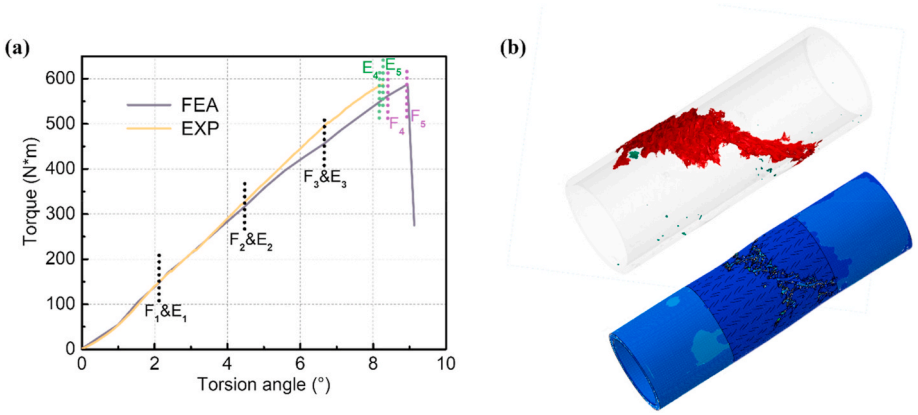

Fig. 3. The torque-torsion angle curve and failure characteristic validate both EXP and FEA. (a) Torque-torsion angle curves. (b) Failure morphology from micro-CT (grey and red image) and FEA (blue).

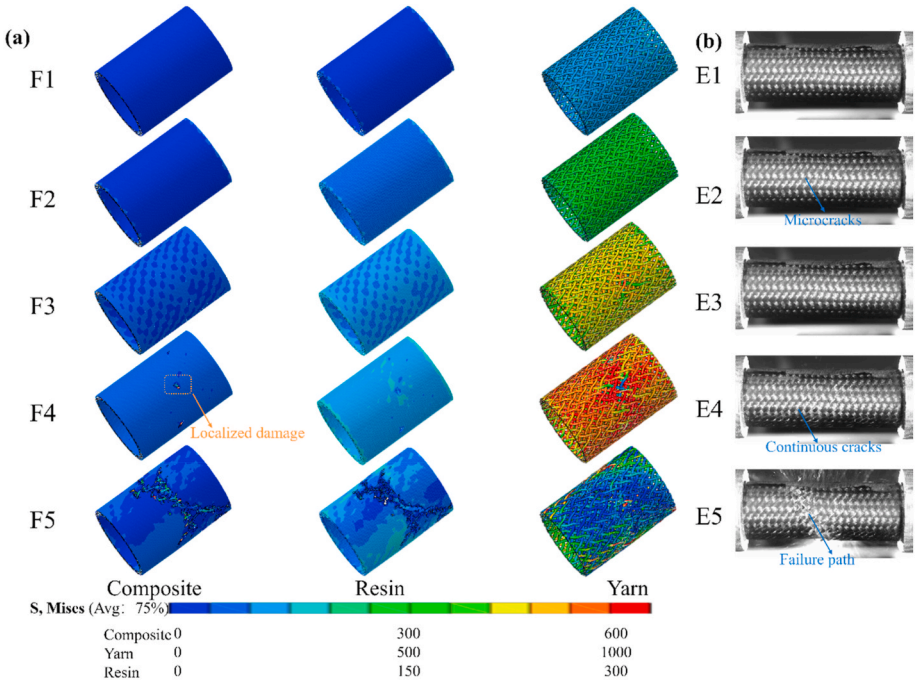

Fig. 4. Spatial progressive damage and surface morphology during torsional loading. (a) Spatial stress distribution from FEA. (b) Photographed surface topography.

torsional behaviors observed in experiments.

4.2. Progressive damage processes

The progressive failure processes are described from morphology and component (resin and yarns) stress distribution, as shown in Fig. 4. Five feature points were selected for detailed investigation, including 1/4, 1/2 and 3/4 of the critical torsion angle, a point just before fracture and the fracture point. These points are labelled E1-E5 for the experiments and F1–F5 for the FEA results, as shown in Fig. 3(a).

In the initial stage of E1-E3, fine resin cracks began to appear on the specimen surface with slight cracking sounds. The distribution of microcracks were scattered. During the E4 stage, the cracking sounds gradually intensified and continuous long cracks occurred. When the torque reached the critical value (E5), the tube instantly fractured in a brittle manner, with a loud "bang" sound. There was a lot of debris flying around. Observations from modelling during the F1–F3 stage revealed no visible deformation in the internal braided yarns and matrix. At the F4 stage, localized damage manifested as yarn deformation and resin cracking. The specimen retained its load-bearing capacity at this point. The damage accumulated rapidly leading to specimen failure when the loading was applied to the F5 moment. The fracture morphology indicated that cracks initially initiated within resin-rich zones between yarns, progressively extending into adjacent interlaced regions along the thickness and braided direction simultaneously.

4.3. Spatial stress analysis

Fig. 5 displays the stress distribution in the composite at the positions of 1/4, 1/2, 3/4 along the axial direction of the meso-scale model component, as well as at the 1/2 axial section. The carbon fiber bundles bear the majority of the torsional stress and their stress increment was greater than that of the resin at each stage, as indicated by the color distribution. Zooming in on the magnified regions, there was a variation in stress distribution between the outer and inner walls for both the resin and the braided yarns. Additionally, an oblique alternating pattern of dark blue and light blue blocks can be observed on the tube wall, indicating a periodic stress distribution.

Outer surface path 1 and inner surface path 2 were selected along the axial direction to evaluate the stress distribution differences, as shown in Fig. 6 (a). The nodal stress distribution exhibits periodic fluctuations, with peaks located in reinforced regions and valleys in resin-rich regions. This emphasize that the stress distribution is dependent on the reinforcement structure. The wave amplitude increased gradually as the feature time increased from F2 to F4. This reveals that the stress gap between the resin and yarn is gradually increasing. It can also be shown that the load-bearing capacity at the inner surface is lower than that at the outer surface at the same time step. At the moment of F4, the mean value of stress on path 1 is 66 MPa, while the mean value of stress on path 2 is 57 MPa.

Fig. 6 (b) provides an in-depth analysis view for exploring the characteristics of the reinforcement structure. A RUC consisting of four yarns was selected and labelled as yarns A, B, C, and D. The yarns A transition from the outside surface unit cell to the inner unit cell, with mean stress shifting from 685.44 MPa to 748.19 MPa. Likewise, yarns D move from the inner unit cell to the internal surface unit cell, undergoing mean stress alteration from 737.67 MPa to 590.83 MPa, respectively. The stress distribution of yarns in the braided structure follows the sequence of inner unit cell > outer surface unit cell > inner surface unit cell. The inner cell, located between the outside and internal surfaces, serves as a bridge for stress transfer. It undergoes bidirectional stress transfer in both inward and outward directions that hinders stress dispersion. Moreover, the fiber density within the inner cell is greater than that in the internal and outside unit cells, further complicating stress transmission. According to Fig. 1(c), the inner unit cell consists of four yarns, while both the internal and outer unit cells consist of two yarns. While the internal surface fibers are closer to the mid-point of the tube for less deformation, which results in lower stress on them. As an individual yarn cycles spatially from the interior to the exterior and back again along the braided path, it has continuous stress changes at various unit cell positions. This leads to stress jumps at unit cell junctions, thereby elevating the risk of yarn breakage.

The complex braided structure also resulted in a staggered distribution of stress and strain, as depicted in Fig. 7. The areas with low stress and high strain are typically situated in the resin-rich gaps between yarns, while areas with high stress and low strain are usually located in the interlaced sections of yarns. Stress concentrations mainly occurred in buckling sections where the fiber bundles interlaced. This is due to the complex interlocking and extrusion bending of the yarn at interlacing points, which inhibits stress propagation from the bending section to the straight section.

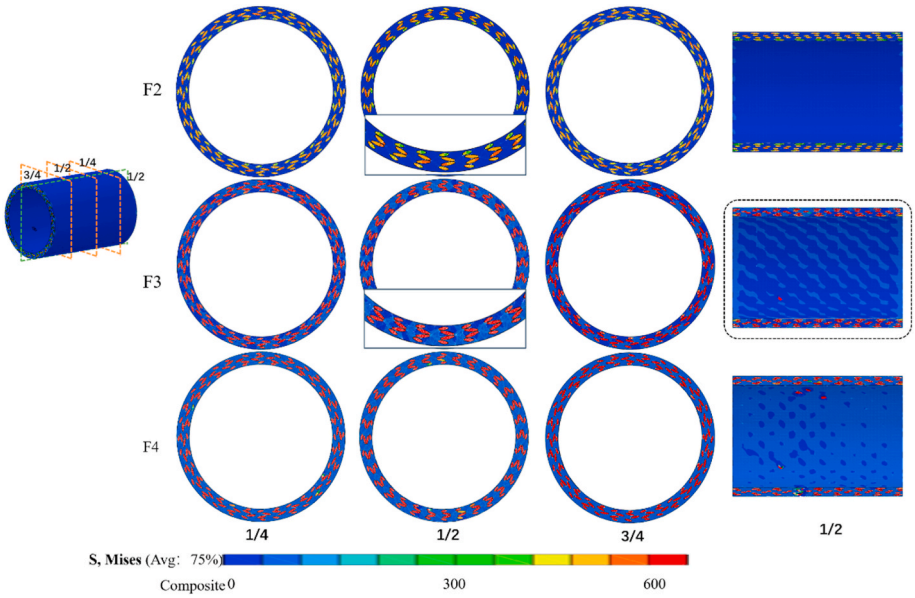

Fig. 5. The stress distribution in the composite at positions located at 1/4, 1/2 and 3/4 along the axial direction and the 1/2 axial section.

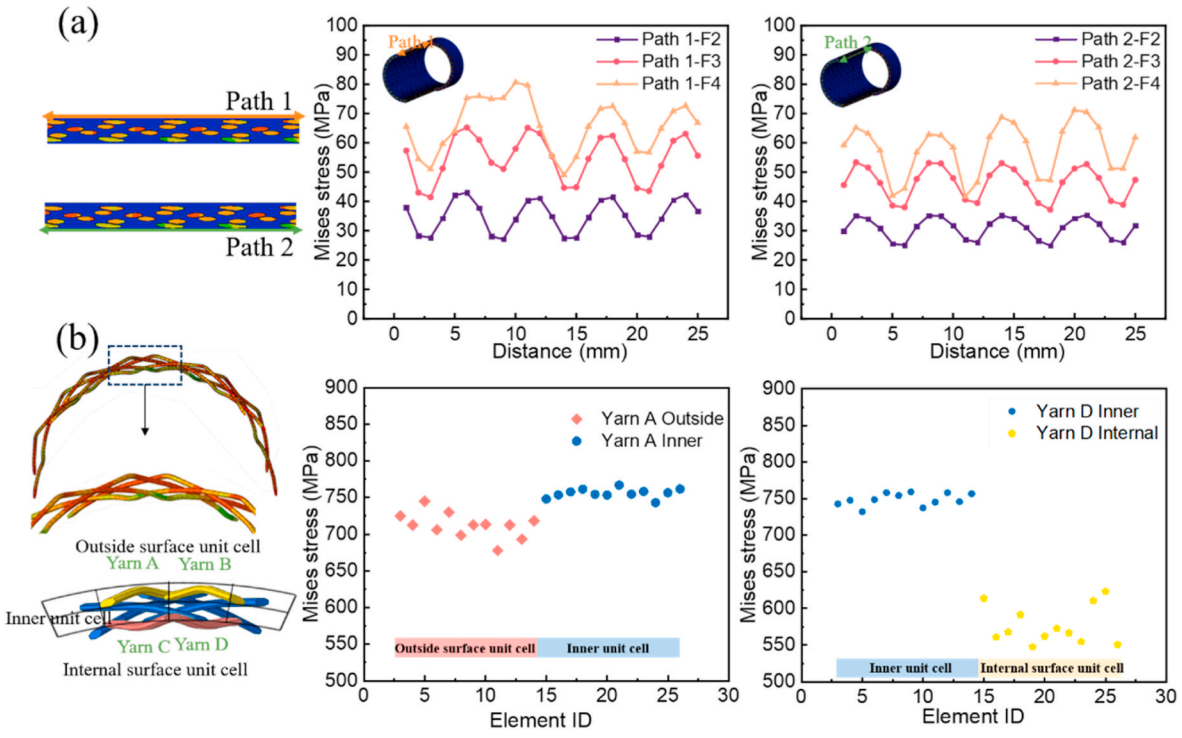

Fig. 6. Differences in stress distribution in resin matrix and yarn reinforcement, respectively. (a) The Mises stress values along Path 1 on the outer surface and Path 2 on the inner surface. (b) Stress analysis in outside unit cell, inner unit cell and internal surface unit cell of a RUC.

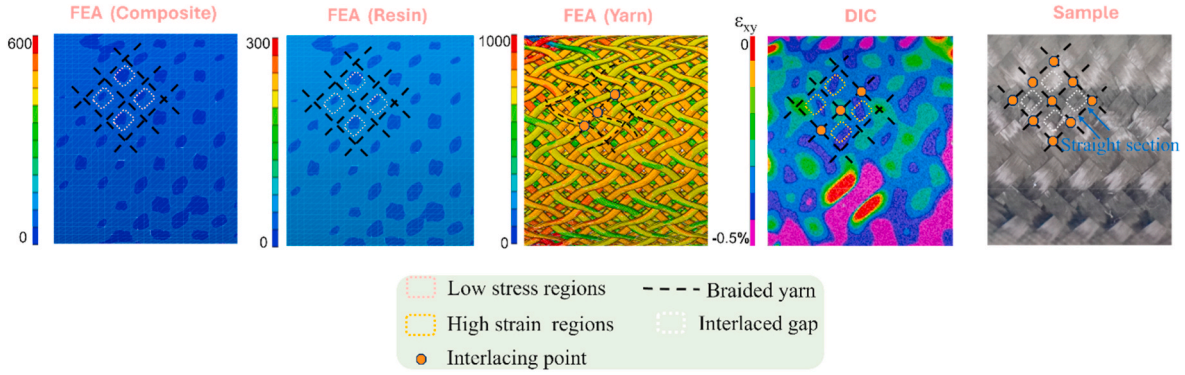

Fig. 7. Characteristics of stress and strain distributions analyzed by FEA, 3D-DIC, and actual tested sample of the braided structures.

4.4. Progressive damage mechanisms

The braided yarns were categorized into two groups, labelled as Group 1 (G1) and Group 2 (G2), based on yarn braiding direction, to reveal damage initiation and propagation mechanisms. G1 was subjected to axial tension in the direction of loading, while G2 experienced axial compression perpendicular to the loading direction (Fig. 8). This implies that the yarns were subjected to both axial compression and axial tension during torsion. Within all braided yarns, the stress magnitudes of G1 and G2 showed that axial tension slightly exceeds axial compression (Fig. 8(b)). At the moment of F4, the G1 stress is 822 MPa, and the G2 stress is 791 MPa. Focusing on the localized region of initial damage, absolute stress levels are extracted in this area, revealing a magnified disparity between axial tensile and compressive stresses (Fig. 8 (c)). Eventually, the gap gradually accumulated over time, resulting in the initial damage in that region. The yarn breakage at the interlacing points extends from the initial damage region to the sides, thus forming a failure path. The failure path aligned with the direction of fiber bundle braiding. This confirms the conclusion drawn in Section 4.2 that the interlacing points of the fiber bundles are more susceptible to failure due to stress fluctuations. The G1 experienced more breakages than G2. The unique braided structure introduces a complex damage propagation path. Also, the interlacing fiber bundles are subjected to axial stresses in both directions simultaneously which aids in stress dispersion and balance. Overall, the mutual interaction of these features limits the damage spreading in 3-D braided structure.

Besides the main form of yarn breakages, other types of yarns damage were analyzed, as shown in Fig. 9. The three categories are deformation, breakage and mixed. Yarns can either remain in their original state or undergo great deformations and splitting (Fig. 9(a)). Yarn break encompasses lapped failure and separation according to the degree of breakage. Yarn breakages consist of different sectional features i.e., neat cuts and oblique untidy cuts. A weak section is susceptible to becoming the subsequent break section, leading to the formation of multiple breakage states (Fig. 9(b)). In Fig. 9(c), the mixed pattern results from the superimposition of multiple damage mechanisms.

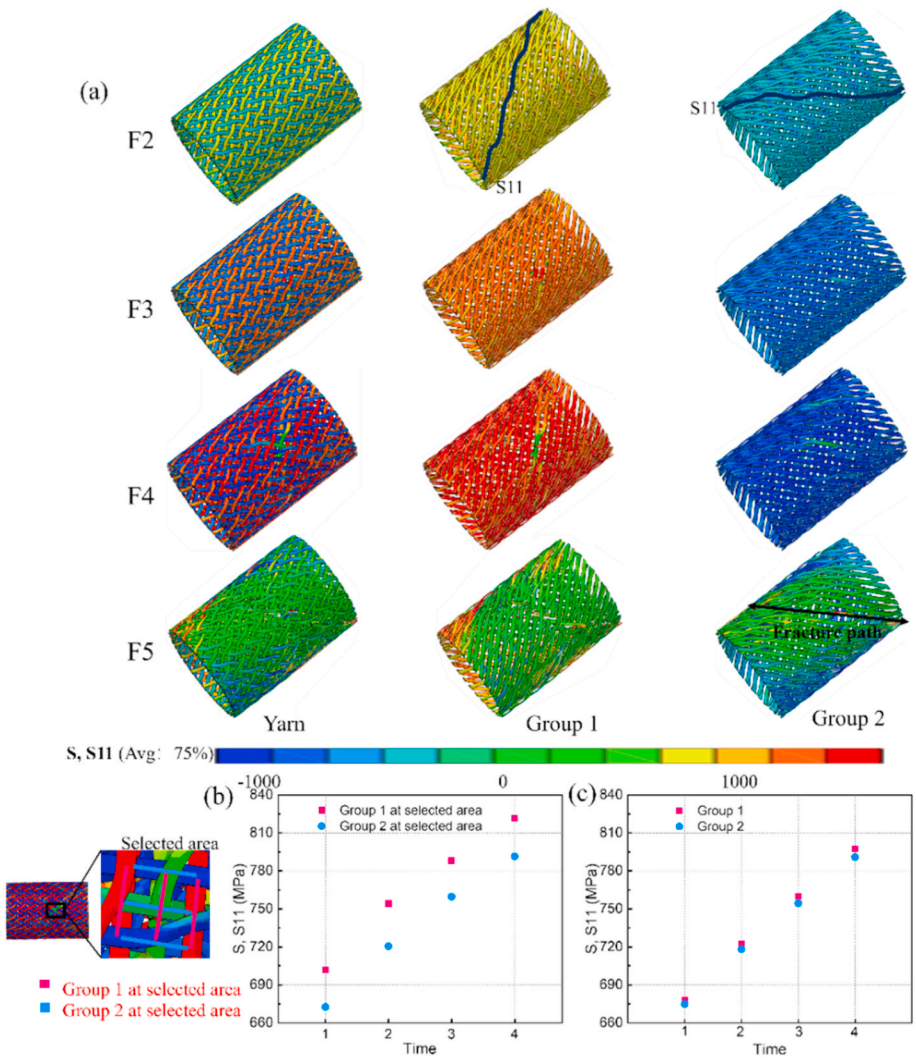

Fig. 8. Progressive damage mechanisms. (a) Spatial stress distribution of interlaced yarns. (b) and (c) S11 stress within the initial damage area and whole braided yarn.

4.5. Interfacial damage propagation

Interfacial damage is typically an important factor when investigating damage progression. Fig. 10 shows the development of interfacial damage at different locations in the axial direction. At F4, interfacial damage first appeared on the inner and outer surfaces and swiftly accumulated and extended inward through the entire tube wall. Damage extended less along radial directions and more along circumferential directions. The nodes' stress-time histories were extracted and graphed to evaluate the impact of interfaces on stress transfer. As shown in Fig. 11 (a) (b), two resin nodes 1 & 2, one braided yarn node and interfaces A & B between resin and yarn were focused on. When the CSDMG value is 0, it indicates that the interface is well bonded at that location. In this case, the stresses applied to the resin and yarns exhibit a continuous linear increase. When the CSDMG reaches 1, the interface cracks. Two conditions were observed: Condition one is when interface A damaged earlier than interface B (Fig. 11(a)). The stress of the braided yarn decreased by 5 %, yet the yarns still have the load-bearing capacity. The stress at resin node 1 started to continuously drop, while node 2 stress continued to grow unaffected by interface A. By the time interface B broke, the braided yarn stress decreased by 63 % and the stress of the resin at node 2 also began to decline. Condition two is when the interfaces A and B failed simultaneously (Fig. 11(b)), causing stress reduction in resin nodes 1 and 2 as well as yarn nodes concurrently.

Disparities in component properties lead to non-uniform deformations, consequently influencing stress transfer and giving rise to local stress concentrations. Interfacial failure occurrences result from interface stress surpassing the interface strength threshold. When the interface is fully bonded, the load applied to the surface is effectively transferred from the resin to the yarn through the interface. The resin and yarn share the interface to carry the loads. The yarn loses contact with the resin once the interface breaks, hindering stress propagation. The analysis of the two interface failure cases reveals that interface damage only affects the stress transfer on both sides of this interface and does not affect the stress transfer in the neighboring interfaces across this damaged interface. That is, damaged interfaces are characterized by localization in hindering stress propagation.

Interfacial damage will distort the stress distribution pattern of yarns. Fig. 12 illustrates the interface damage and stress distribution of yarns within a unit cell. The interface damage corresponds to the stress transition regions. In Fig. 12(b), two interface damages are observed at the stress trough (F3). The interface damage gradually extends under loading over time (F4), disrupting the stress transfer of the yarns. Eventually, the accumulation of interface damage results in the yarn failure (F5).

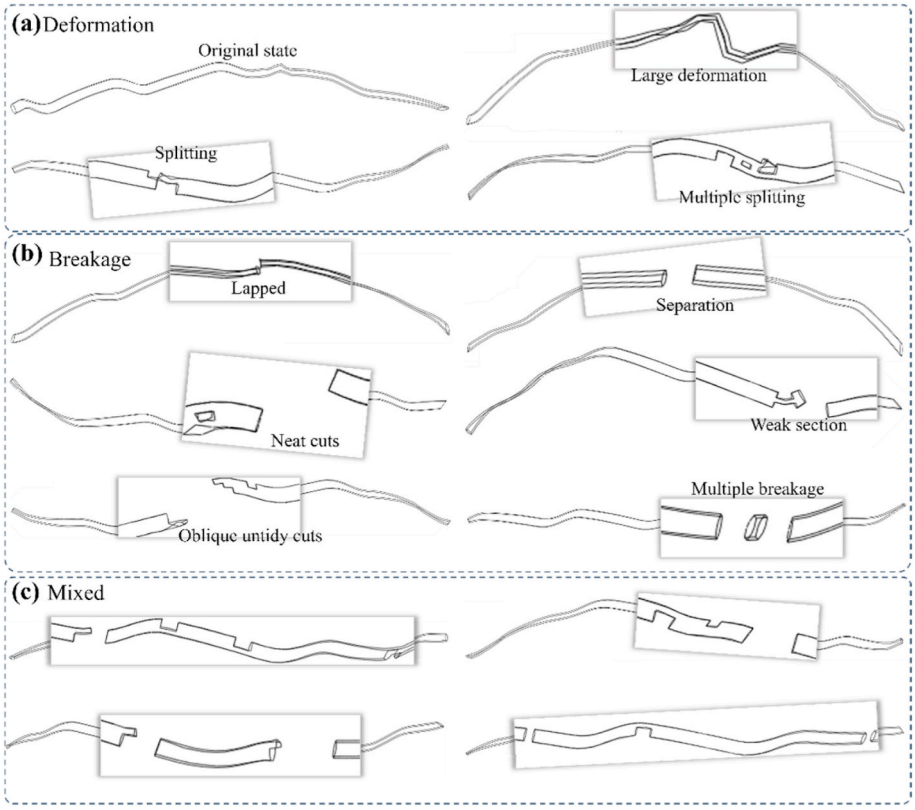

Fig. 9. Failure patterns in yarns. (a) Buckling deformation. (b) Fracture. (c) Mixed damage.

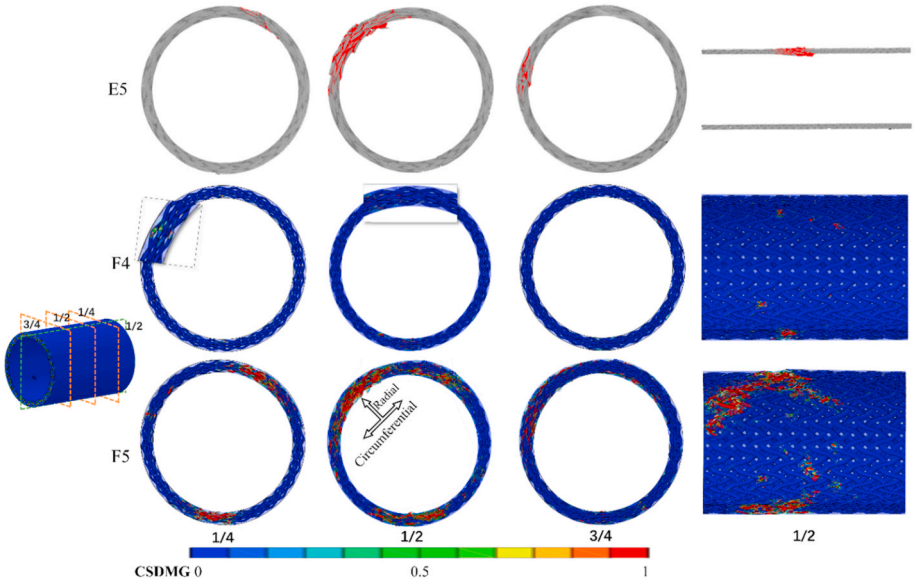

Fig. 10. Evolution of yarn/resin interfacial damage at positions located at 1/4, 1/2 and 3/4 along the axial direction and the 1/2 axial section from FEA and Micro-CT.

5. Conclusions

The present paper reports the torsional progressive failure mechanisms of 3-D braided composite tubes. An equivalent hybrid model combining mesoscale modelling around the damage region and macroscale homogenization away from the damage region was proposed to analyze spatial stress distribution and interfacial damage propagation. The strain evolution and reconstructed failure morphologies obtained from experiments by using 3D-DIC and micro-CT supported the FEA.

It was found that there is non-uniform spatial stress distribution in braided tubes because the load-bearing capacity differences between resin and carbon fibers. The interlacing points of braided fibers are subjected to stress concentration due to buckling. Additionally, the braided fiber bundles experience continuous periodic stress fluctuations at different unit cell positions within an RUC. The yarn stress is highest when the yarn passes through the inner unit cell, lower when it passes

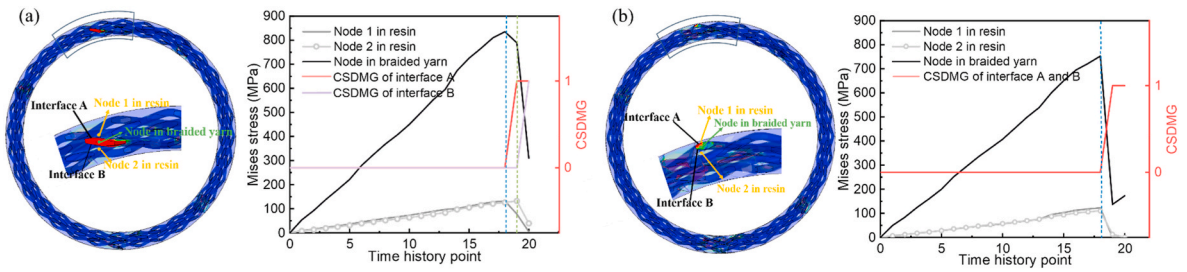

Fig. 11. Interfacial damage morphologies and stress-time history at resin nodes 1&2, braided yarn node and interfaces A & B. (a) Interface A failed earlier than interface B. (b) Interfaces A and B failed simultaneously.

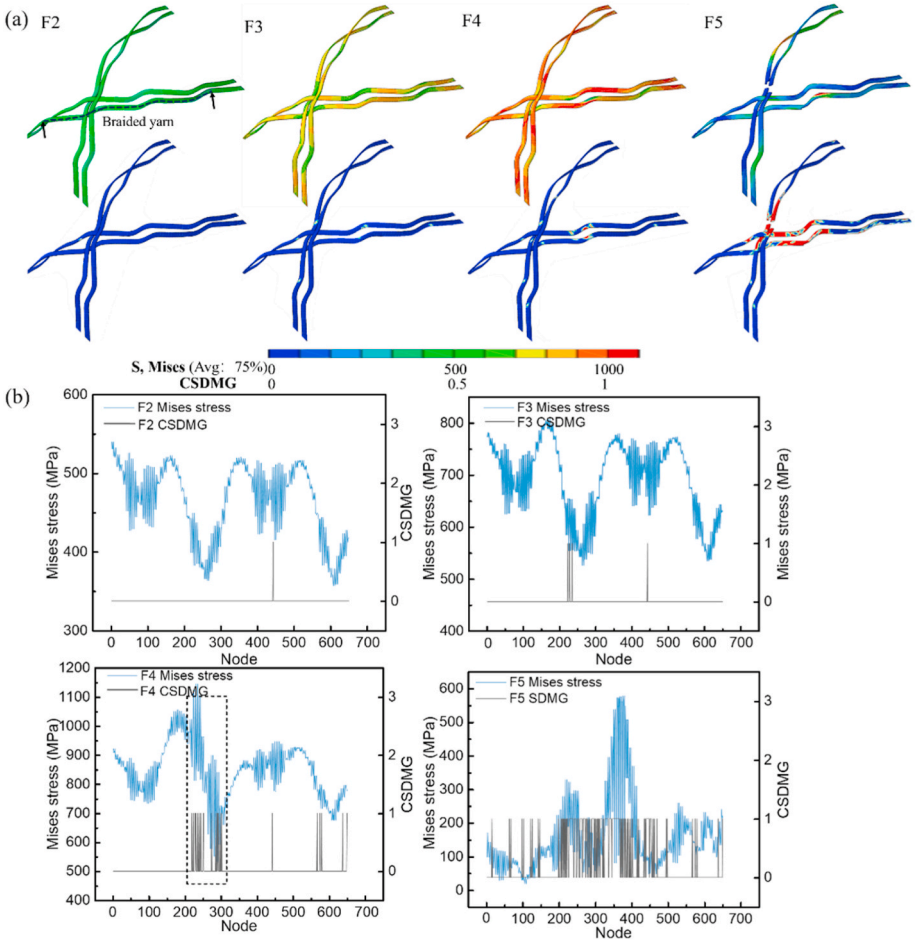

Fig. 12. Relation between stress distribution and interfacial damage progression. (a) Stress and CSDMG distribution within an unit cell. (b) Stress and CSDMG variation curves for selected braided yarn with feature time.

through the outer surface unit cell and lowest when it passes through the inner surface unit cell. The yarns undergo both axial compression and axial tension during torsion. The stress differences between compression and tension gradually accumulate over time, resulting in initial damage which extends to the sides, eventually forming a failure path along interlacing points.

We also found that the interface cracking due to differences in stress distribution is the main torsional damage mode. Damaged interfaces hinder efficient stress transfer between the fiber bundle and resin, disrupting the regular stress propagation pattern on the fiber bundles. The damage propagation becomes trapped among fiber bundles due to the complex braided paths, axial stress dispersion in two directions and multi-scale structural characteristics. This enhances the damage tolerance and highlights the superiority of the 3-D braided structure.

CRediT authorship contribution statement

Limeng Xun: Investigation, Writing – original draft. **Yasmine Mosleh:** Formal analysis, Methodology. **Baozhong Sun:** Project administration, Resources, Supervision. **John-Alan Pascoe:** Supervision. **Bohong Gu:** Funding acquisition, Supervision, Writing – original draft, Writing – review & editing.

Declaration of competing interest

The authors declare that they have no known competing financial interests or personal relationships that could have appeared to influence the work reported in this paper.

Data availability

Data will be made available on request.

Acknowledgements

This work was supported by the National Science Foundation of China (Grant Number 12372130), the Fundamental Research Funds for the Central Universities and Graduate Student Innovation Fund of Donghua University (Grant Number CUSF-DH-D-2022032), and the China Scholarship Council (CSC) fund (No. 202206630032).

References

[1] Q.J. Gu, Z.Z. Quan, J.Y. Yu, J.H. Yan, B.Z. Sun, G.B. Xu, Structural modeling and mechanical characterizing of three-dimensional four-step braided composites: a review, Compos. Struct. 207 (2019) 119–128.
[2] Y. Liu, T.W. Chou, Additive manufacturing of multidirectional preforms and composites: from three-dimensional to four-dimensional, Mater. Today Adv. 5 (2020).
[3] Y. Ke, B. Sun, B. Gu, W. Zhang, Damage initiation and propagation mechanisms of 3-D angle-interlock woven composites under thermo-oxidative aging, Compos. Struct. 259 (2021) 113462.
[4] Y. Wu, W. Cao, J. Guo, L. Xun, B. Sun, B. Gu, Near-fiber nanomechanical mapping and impact failure mechanism of 3D braided composites subjected to thermo-oxidative environment, Compos. Sci. Technol. 216 (2021) 109052.
[5] Y. Wu, J. Guo, L. Xun, B. Sun, B. Gu, Anisotropic degradation mechanism on low-velocity impact of 3D braided composites after thermo-oxidative ageing, Thin-Walled Struct. 182 (2023) 110204.
[6] Y. Wu, L. Xun, S. Huang, C. Ren, B. Sun, B. Gu, Crack spatial distributions and dynamic thermomechanical properties of 3D braided composites during thermal oxygen ageing, Compos. Appl. Sci. Manuf. 144 (2021) 106355.
[7] J. Ke, L-j Liu, Z-y Wu, Z-p Le, L. Bao, D-w Luo, Torsional mechanical properties and damage mechanism of glass fiber-ramie hybrid circular tube, Compos. Struct. 327 (2024) 117680.
[8] Y. Chang, W. Wen, Y. Xu, H. Cui, Y. Xu, Quasi-static mechanical behavior of filament wound composite thin-walled tubes: tension, torsion, and multi-axial loading, Thin-Walled Struct. 177 (2022) 109361.
[9] W.Z. Zhao, N. Pei, C.G. Xu, Experimental study of carbon/glass fiber-reinforced hybrid laminate composites with torsional loads by using acoustic emission and Micro-CT, Compos. Struct. 290 (2022).
[10] A. Armanfard, G.W. Melenka, Experimental evaluation of carbon fibre, fibreglass and aramid tubular braided composites under combined tension-torsion loading, Compos. Struct. 269 (2021).
[11] Y. Chai, Y. Wang, Z. Yousaf, M. Storm, N.T. Vo, K. Wanelik, et al., Following the effect of braid architecture on performance and damage of carbon fibre/epoxy composite tubes during torsional straining, Compos. Sci. Technol. (2020) 200.
[12] J. Holmes, S. Sommacal, R. Das, Z. Stachurski, P. Compston, Digital image and volume correlation for deformation and damage characterisation of fibre-reinforced composites: a review, Compos. Struct. 315 (2023).
[13] Y.H. Gu, D.T. Zhang, Z.W. Zhang, J. Sun, S.L. Yue, G. Li, et al., Torsion damage mechanisms analysis of two-dimensional braided composite tubes with digital image correction and X-ray micro-computed tomography, Compos. Struct. 256 (2021) 113020.
[14] G.W. Melenka, J.P. Carey, Experimental analysis of diamond and regular tubular braided composites using three-dimensional digital image correlation, J. Compos. Mater. 51 (2017) 3887–3907.
[15] W.F. Hao, Z.R. Yuan, C. Tang, L. Zhang, G.Q. Zhao, Y. Luo, Acoustic emission monitoring of damage progression in 3D braiding composite shafts during torsional tests, Compos. Struct. 208 (2019) 141–149.
[16] G.Q. Zhao, L. Zhang, C. Tang, W.F. Hao, Y. Luo, Clustering of AE signals collected during torsional tests of 3D braiding composite shafts using PCA and FCM, Compos. B Eng. 161 (2019) 547–554.
[17] G.Q. Zhao, L. Zhang, B. Wang, W.F. Hao, Y. Luo, HHT-based AE characteristics of 3D braiding composite shafts, Polym. Test. 79 (2019) 106019.
[18] G.W. Melenka, E. Lepp, B.K.O. Cheung, J.P. Carey, Micro-computed tomography analysis of tubular braided composites, Compos. Struct. 131 (2015) 384–396.
[19] H.Q. Ali, A. Kheyabani, C. Akalin, A. Kefal, M. Yildiz, Numerical and experimental methodologies to investigate the damage progression inside the axisymmetric composite cylinders with cutouts under torsion, Compos. Struct. 315 (2023) 116990.
[20] B.H. Shi, M. Zhang, S.K. Liu, B.Z. Sun, B.H. Gu, Multi-scale ageing mechanisms of 3D four directional and five directional braided composite's impact fracture behaviors under thermo-oxidative environment, Int. J. Mech. Sci. 155 (2019) 50–65.
[21] C. Hang, H. Cui, H.F. Liu, T. Suo, Micro/meso-scale damage analysis of a 2.5D woven composite including fiber undulation and in-situ effect, Compos. Struct. 256 (2021).
[22] L. Ge, H.M. Li, J.H. Zhong, C. Zhang, D.N. Fang, Micro-CT based trans-scale damage analysis of 3D braided composites with pore defects, Compos. Sci. Technol. (2021) 211.
[23] A. Gholami, G.W. Melenka, Studying the geometrical models of tubular braided composite using micro computed tomography and particle swarm optimization, Compos. B Eng. 260 (2023).
[24] D.H. Kim, S.W. Kim, Prediction of effective mechanical properties of 2D triaxially braided composites using a geometrical model incorporating flat portions of composite yarns, Mater. Today Commun. 35 (2023).
[25] J. Zhai, T. Zeng, G.D. Xu, Z.H. Wang, S. Cheng, D.N. Fang, A multi-scale finite element method for failure analysis of three-dimensional braided composite structures, Compos. B Eng. 110 (2017) 476–486.
[26] Y.Y. Zhang, H.M. Li, Y.H. Gao, R.S. Lou, L. Ge, D.N. Fang, Multi-scale modeling and elastic properties prediction of 3D four-directional tubular braided composites, Compos. Struct. 292 (2022) 115632.
[27] W.F. Hao, Z. Huang, L. Zhang, G.Q. Zhao, Y. Luo, Study on the torsion behavior of 3-D braided composite shafts, Compos. Struct. 229 (2019) 111384.
[28] Y. Wang, Z.G. Liu, Y.P. Yi, Y.C. Wei, Z.J. Li, Y.B. Wang, Damage and failure analyses of 3D4d braided composite shafts under torsional load and the effects of braid processing parameters on their torsional properties, Polym. Compos. 42 (2021) 1912–1944.
[29] L.H. Gong, X.H. Gao, H. Yang, Y.H. Liu, X.F. Yao, Design on the driveshaft of 3D 4-Directional carbon fiber braided composites, Compos. Struct. 203 (2018) 466–473.
[30] A. Armanfard, G.W. Melenka, Experimental evaluation of carbon fibre, fibreglass and aramid tubular braided composites under combined tension–torsion loading, Compos. Struct. 269 (2021) 114049.
[31] P. Potluri, A. Manan, M. Francke, R.J. Day, Flexural and torsional behaviour of biaxial and triaxial braided composite structures, Compos. Struct. 75 (2006) 377–386.
[32] Z.-M. Huang, A bridging model prediction of the ultimate strength of composite laminates subjected to biaxial loads, Compos. Sci. Technol. 64 (2004) 395–448.
[33] Z.M. Chen, C.M. Yue, Y. Zhang, P. Wang, Y.Y. Li, Z.Q. Gu, Thermo-mechanical response of 3D braided composites with different braiding angles under high strain rate punch shear loading, J. Compos. Mater. 56 (2022) 3603–3616.